Engineering Structures 334 (2025) 120206

Contents lists available at ScienceDirect

Engineering Structures

journal homepage: www.elsevier.com/locate/engstruct

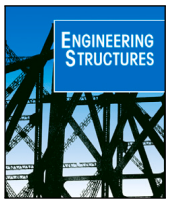

A temperature compensation method to consider the effects of thermal inertia in anomaly detection schemes

S. Mariani *, F. Zeighami, A. Kalantari, S. Kamali, S. de Miranda, A. Marzani

Department of Civil, Chemical, Environmental and Materials Engineering — DICAM, University of Bologna, Viale del Risorgimento 2, Bologna, 40136, Italy

ARTICLE INFO

Keywords:
Thermal Inertia
Temperature compensation
Thermomechanics
Damage detection
MLR
KW51

ABSTRACT

The effects of materials' thermal inertia need to be considered when deploying temperature compensation methods for anomaly detection in structural health monitoring. This article presents a method based on multiple linear regression between sequences of temperature and structural response that addresses this problem by taking into account the time delay effects induced by thermal inertia. Such method is first thoroughly evaluated on two numerical datasets, each consisting of temperature measurements acquired at a single structural location paired with either a "global" structural parameter (i.e., a natural frequency of vibration) or a "local" one (i.e., strain). Both datasets are generated via a finite element model of an aluminum beam-like structure in which heat transfer and structural analyses are coupled. Two types of damage are considered: a local reduction of the Young's modulus of the material and a differential settlement. The effects of thermal inertia on the measured global and local structural responses are discussed, and the algorithm's ability to capture these effects is evaluated. Then, the method is applied to some open-access experimental modal data acquired from the well-known KW51 railway bridge. In all considered scenarios, the method strongly outperforms the widely used linear regression between "instantaneous" pairs of temperature and structural measurements. Notably, the results demonstrate that by considering sufficiently long histories of temperature measurements, the information from even a single thermocouple can accurately predict both global and local structural responses when only thermal loads are present.

1. Introduction

Data-driven systems for structural health monitoring (SHM) of large civil structures make use of a limited number of sensors deployed at various locations and measuring structural responses, such as accelerations or strains, and environmental factors, such as temperature or humidity, at given sampling rates [1]. Typically, the goal is to set an automated analysis framework that assesses the structural integrity by inspecting the recorded signals [2,3]. The detection of damage-related signatures within the measured time-series is hindered by the effects of environmental and operational variations, which can often mask subtler structural changes caused by damage [4]. Among the possible environmental agents, temperature typically has the largest effect on the structural response [4]. In fact, the changes induced by temperature can often exceed those due to operational variations, such as vehicular traffic in bridges [5–7].

Large structures are subjected to thermal loads deriving from the diurnal and seasonal temperature variations. Some of their surfaces are exposed to direct solar radiation, while convective and radiative phenomena with surrounding air and objects occur at all external surfaces. Under these boundary loads, heat conduction occurs internally. This is regulated by the geometry of the structure and the thermal inertia of the materials, defined as their property to resist changes in their temperature due to their heat capacity and thermal conductivity [8]. Due to the constantly varying thermal loads acting at the boundaries, non-uniform temperature distributions within the structure exist at any instant of time. This internal distribution generates local variations in the material properties as well as thermally-induced strains and stresses [9]. Such non-uniform temperature field is responsible for the time lags that are often observed between the recordings of temperature and structural response [10,11].

Since the conductive heat transfer phenomena occurring in large structures can require tens of minutes, if not hours, to fully unravel [10,12,13], it appears necessary to analyze sufficiently long temperature sequences for successful regressions between these and structural responses. Once an effective regression is trained, it can then be used to predict and remove the effects of varying temperature on the measured structural responses. To the best of the authors knowledge, Sohn et al. [14] were the first to propose the use of multiple temperature

* Corresponding author.
E-mail address: stefano.mariani9@unibo.it (S. Mariani).

https://doi.org/10.1016/j.engstruct.2025.120206
Received 20 November 2024; Received in revised form 20 February 2025; Accepted 25 March 2025
Available online 9 April 2025

data acquired at different time instants to train a regressor between temperature and structural response (in their case, modal parameters). However, they only considered including a single past temperature reading in addition to that acquired at the same time instant of the structural response. While their study used multiple linear regression (MLR) [15], two years later Peeters and De Roeck [16] setup an ARX model [17] to perform an analogous task. Again to the best of the authors knowledge, no other works have reported the use of temperature data acquired at multiple time instants for the following fifteen years, when Kromanis et al. [18] proposed to include a single past temperature data in order to predict strain measurements. Five years later, Wang et al. [19] presented an approach using a long short-term memory (LSTM) algorithm [20] fed with temperature and deflection measured at six different time instants to model the expected deflection of a suspension bridge. Recently, some of the authors of this article have proposed the use of multiple regressors fed with a large number of temperature measurements acquired by a single sensor to predict strain gauge readings [21]. The extent of that investigation was limited by difficulties in getting access to experimental datasets featuring a frequent and continuous acquisition of both temperature and structural response, and also including the formation of damage. Therefore, the method was tested on a monitoring dataset that had been collected on a laboratory truss structure for a different scope [18], which only exhibited very short time lags between temperature and strain since the structure was almost uniformly heated by infrared lamps.

In this work, the above mentioned difficulties are overcome by using numerical datasets generated via finite element (FE) modeling. In particular, two synthetic monitoring scenarios are simulated, a dynamic one based on modal parameters and a quasi-static one based on the measurement of strain, both of which exhibiting significant non-uniform temperature distributions varying over time and featuring the introduction of damage. This allows (i) evaluating whether the temperature compensation method first introduced in [21] is also able to predict "global" structural responses, such as natural frequencies of vibrations, and (ii) investigating the effects of measurement noise on such method by comparing the results obtained when applying the method to either noiseless or noise-added data. Finally, the applicability of the proposed method to real-world modal data is evaluated by applying it to the open-access dataset acquired from the KW51 railway bridge [22].

The remainder of the article is structured as follows. Section 2 describes the temperature compensation method based on sequential temperature measurements that is later evaluated on both simulated and experimental monitoring scenarios. The FE model used to generate the numerical datasets is presented in Section 3, while Section 4 discusses the application of the proposed algorithm to such datasets. Section 5 presents the results obtained on the experimental dataset, before Section 6 concludes the article by highlighting the key findings.

2. Temperature compensation method based on sequential temperature measurements

As for the vast majority of the temperature compensation methods available in literature [4], the proposed method requires the collection of measurements from the monitored structure over an initial "baseline" period. Such baseline dataset is used to train a regression model between temperature and structural response. The trained model is then used in a subsequent "monitoring" phase to remove temperature effects, so that non-temperature-related deviations from the baseline structural conditions can be more easily detected.

Crucially, the novel assumption of the proposed method is that the structural response can only be predicted in a satisfactory manner if sufficiently long sequences of temperature measurements are paired with the structural response expected at the end of such sequences. The duration of the sequences should be long enough as to fully capture the heat transfer phenomena occurring within the structure, which are regulated by the materials' thermal inertia. Note that this approach is radically different than that widely seen in literature (e.g., [23]), in which temperature reading(s) acquired by one or multiple thermocouples at a single instant of time are related to the structural response measured at the same time instant.

Table 1
Aluminum properties sampled from the higher degree polynomial functions of temperature available in COMSOL Multiphysics® [26]. T, E, ν and α stand for temperature, Young's modulus, Poisson's ratio and thermal expansion coefficient, respectively.

T [°C]	20	25	30	35	40	45	50
E [GPa]	69.14	68.97	68.79	68.62	68.45	68.28	68.11
ν [–]	0.3312	0.3313	0.3314	0.3315	0.3316	0.3317	0.3318
α [10^{-6} °C^{-1}]	22.23	22.33	22.44	22.54	22.64	22.74	22.84

In [21] both MLR and a deep learning-based multiple regressor were tested over an experimental dataset, and the results showed that the deep learning (DL) technique was only slightly superior to MLR though requiring significantly higher computational costs. Another DL technique that is well-versed for the analysis of sequential data is LSTM, possibly used in combination with convolutional neural networks to combat the notorious LSTM's vanishing gradient problem as suggested in [24], but such approach would also require significant computational costs. For these reasons, this article uses MLR as the multiple regressor of choice. This is expressed as:

$$Y = \alpha + \beta_0 X_0 + \beta_1 X_1 + \cdots + \beta_n X_n + \xi \tag{1}$$

where Y is the dependent variable, $X_0, X_1, \ldots, X_n$ are $n+1$ multiple independent variables, $\beta_0, \beta_1, \ldots, \beta_n$ are the corresponding coefficients that measure the impact of each independent variable on the dependent variable, α is the intercept term, and ξ is the error term that captures the unexplained variation in the data. In this work, Y is the measured structural response and $X_0, X_1, \ldots, X_n$ are sequential temperature measurements acquired by a single thermocouple. In particular, X_0 is the temperature measured simultaneously as Y, X_1 is the temperature measured at the previous sample in time, and so for up to X_n being the temperature measured n samples in the past. α and β_i coefficients are estimated via least squares fitting over the "baseline" dataset. Note that Eq. (1) reduces to linear regression (LR) when only a single independent variable X_0 is used.

In this study, the metrics that is used to evaluate the predictive performance of a trained MLR model over a given set of m structural responses is the coefficient of determination R^2 [25], which is defined as:

$$R^2 = \left(1 - \frac{\sum_{i=1}^{m}(Y_i - \hat{Y}_i)^2}{\sum_{i=1}^{m}(Y_i - \bar{Y})^2}\right) \cdot 100 \tag{2}$$

where Y_i is the ith value of the measured structural response, $\hat{Y}_i$ is its prediction by MLR, and $\bar{Y}$ is the mean of the m measured structural responses, i.e., $\bar{Y} = \frac{1}{m}\sum_{i=1}^{m} Y_i$.

3. Numerical case studies

The algorithm of Section 2 is first investigated over two numerical case studies, termed C1 and C2. In each of them, an aluminum 0.1×0.1×1 m beam (Fig. 1) having temperature-dependent material properties (Table 1) is subjected to the same set of boundary conditions (BCs) for the heat transfer analysis, while different mechanical BCs are applied, as summarized in Table 2. With regards to the structural analysis, in C1 the structure is fixed throughout Boundaries 1 and 6 (Fig. 1), while in C2 the four corner nodes of Boundary 1 are constrained. For both case studies, the structural initial displacement and velocity fields are null everywhere.

The right columns of Tables 2 and 3 list BCs and initial conditions, respectively, employed for the heat transfer analysis. The initial temperature is set to 20 °C throughout the structure, then heat is injected

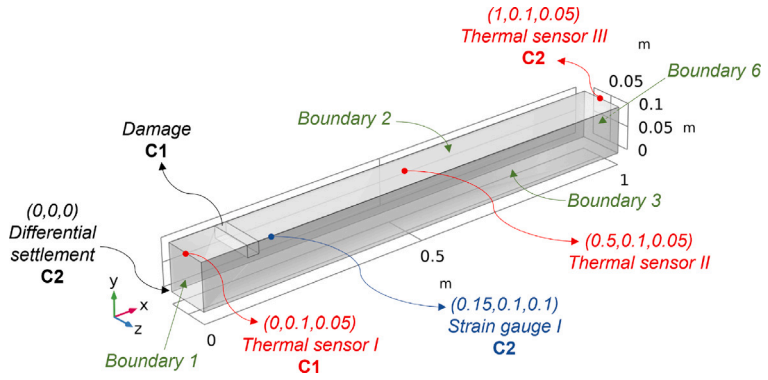

Fig. 1. Geometry of the modeled beam-like structure. All measures are in meters. "C1" and "C2" indicate features considered in either case study C1 or C2, respectively. The origin of the reference system is at the bottom left corner of Boundary 1. This is also the corner being displaced in case study C2 to simulate a differential settlement. Boundaries 4 and 5, not labeled in figure, are opposite to Boundaries 2 and 3, respectively.

Table 2
Boundary conditions used in case studies C1 and C2. Boundary numbers refer to Fig. 1.

Boundary	Structural mechanics		Heat transfer
	C1	C2	
1	Fixed	Fixed corners	Insulated
2	Free	Free	Convection
3	Free	Free	Convection
4	Free	Free	Convection
5	Free	Free	Convection
6	Fixed	Free	Specified heat

Table 3
Monitored parameters, type of damage and initial conditions considered in case studies C1 and C2.

	Structural mechanics		Heat transfer
	C1	C2	
Monitored parameters	Eigenfrequencies	Strain	Temperature
Damage	Reduction of Young's modulus	Differential settlement	-
Initial conditions	Null-displacements Null-velocities		20 °C

through Boundary 6 in Fig. 1 by specifying a time-dependent inward heat flux for a total duration of 192 h, which is also the total simulation time. The prescribed history of heat flux is obtained by repeating a 6 hour-long period having 180 min of increasing inward heat up to a maximum of 6000 W/m^2, followed by 3 min of rapid decrease and 177 min of null-inward heat. The first two periods are shown in Fig. 2. This pattern loosely mimics a time-scaled repeating diurnal pattern where solar radiation heats up a structure for roughly half a day. Convection to surrounding air was simulated at Boundaries 2 to 5 by setting the convective heat transfer coefficient to 5 W/(m^2 · °C) and the air's temperature to 20 °C throughout the simulation time (see Eq. (A.3) in Appendix). The chosen convection heat transfer coefficient h^c is in line with some experimentally estimated values for metal structures in the absence of wind [27]. Finally, Boundary 1 is thermally insulated, i.e., its inward/outward heat is set to 0 along the whole simulation time.

3.1. Case study C1

In case study C1 the thermal sensor was positioned at (0,0.1,0.05) m, i.e., at the furthest distance from the specified inward heat, and an eigenfrequency study was run in parallel to the transient analysis in order to compute the first four eigenfrequencies. This simulates the deployment of a single or multiple accelerometers across the structure that capture ambient-induced vibrations, which are then used to estimate structural modal parameters via operational modal analysis (OMA) [28]. A 5% reduction of the temperature-dependent Young's modulus of Table 1 was assigned to a $0.025 \times 0.025 \times 0.1$ m portion of the modeled beam after 143 h of simulation time, i.e., towards the end of the 24th repeating heating period. Such portion is at a distance of 0.1 m from Boundary 1, and its exact location is visible in Fig. 1 (where it is labeled "Damage"). Physically, a local rigidity loss can be caused by the insurgence of some damage at that location. The induced reduction of the overall structural stiffness results in slightly lowered eigenfrequencies.

3.2. Case study C2

In case study C2 temperature was measured at (1,0.1,0.05) m, i.e., at one of the edges of Boundary 6 through which the specified heat flux enters the structure. This mimics positioning a thermocouple at a sun-facing surface of an outdoor structure. A strain gauge measuring axial strains in the x-direction was positioned at (0.15,0.1,0.1) m. Then, a differential settlement at the clamped end of the structure was simulated to occur after 143 h of simulation time. This was modeled by imposing a 1 mm displacement at the corner labeled "Differential settlement" in Fig. 1 along the negative x direction, while the other three corners of Boundary 1 were kept at their fixed initial positions. This induces a local distribution of strains and stresses, which fades moving away from the clamped end of the beam. The exact location of the strain gauge was deliberately chosen as to be only moderately sensitive to the effects of such distribution.

3.3. Finite element implementation

The data of the two case studies described above were generated via FE modeling in COMSOL Multiphysics®. A one-way coupled thermal/structural transient analysis, where the former influences the latter at each integration time-step (see Appendix), was performed using the implicit Backward Differentiation Formula (BDF) time stepping method of order 2 and the PARDISO direct solver [29]. The model was set to store the results and to perform the eigenfrequency analysis (only for C1) at a constant time-interval of 60 s, which defines the sampling interval used for all measurements described above. A mesh refinement study lead to the use of a regular hexahedral mesh formed by 640 cubic elements with sides of 0.025 m and having quadratic lagrangian shape functions for both heat transfer and structural analyses.

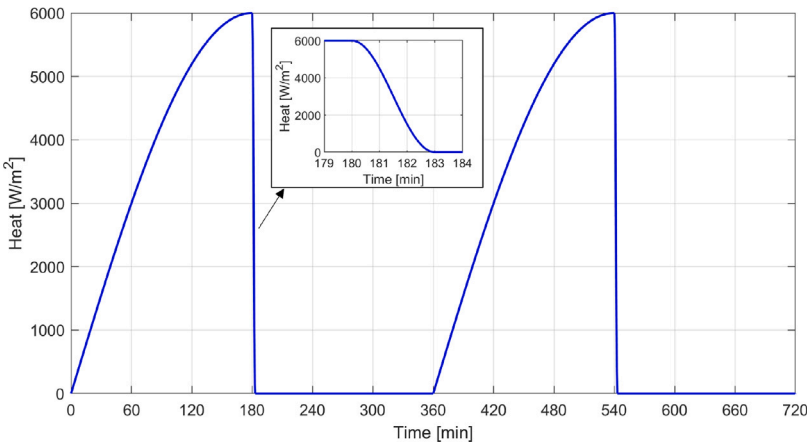

Fig. 2. First two periods of the cyclic history of inward heat flux injected through Boundary 6. The inset plot zooms in the 179–184 min range to better show the period during which the inward flux decreases.

4. Results from the numerical case studies

4.1. Temperature field

Fig. 3(a) shows the temperature measured by "thermal sensors I to III" of Fig. 1 across the simulation length of either case study C1 or C2 (since their heat transfer solutions are identical). After about three heating periods the structure reaches a state of "dynamic" thermal equilibrium between the cyclically injected heat flux and convection losses to surrounding air. At that stage, thermal sensor III, which is located at the boundary where heat enters the structure, approximately experiences a 19 °C excursion, while thermal sensors II and I are subjected to much attenuated thermal variations of about 7 and 5 °C, respectively. Furthermore, the zoomed view of Fig. 3(b) clearly shows the differences in the three signal shapes, notably the presence of increasingly more delayed and widely spread temperature "peaks" and "valleys" together with smoother heating and cooling phases as one moves away from the source of heat. This behavior is a direct consequence of the "smoothing" nature of diffusion equations such as Eq. (A.1) in Appendix (see e.g., [30]). Finally, Fig. 3(c) depicts the temperature field after 45 h of simulations, i.e., in correspondence to the green dashed vertical line of Fig. 3(b), giving a visual representation of the non-uniform temperature distribution existing at any instant of time.

4.2. Case study C1: modal data

The lowest four eigenfrequencies of the modeled doubly clamped beam correspond to the two pairs of first- and second-order bending modes, whose modal shapes are displayed in Fig. 4(c). In particular, the first and second modes vibrate at the same frequency and correspond to the first-order bending resonance, with displacements occurring in either of the two orthogonal planes, $x - y$ and $x - z$. Similarly, the third and fourth modes correspond to the second-order bending resonance, with displacements polarized in either the $x-y$ or $x-z$ plane. In the "dynamic" thermal equilibrium phase reached after ~18 h of simulation time, the first-order bending modes vary with temperature in the ~488.5–491.5 Hz range, while the second-order bending modes are in the ~1254.5–1260 Hz range. This is shown in Fig. 4(a), where the four eigenfrequencies are plotted over a 12 h period centered at the time of introduction of damage. The stiffness reduction occurring at 143 h induces small downward shifts in all four modal frequency traces. This is better seen in Fig. 4(b), which zooms in the region indicated by the black rectangle in Fig. 4(a). For each pair of bending modes, the largest shift occurs for the $x - y$ polarization (i.e., for "Mode 1" and "Mode 3", as displayed in Fig. 4(c)). Only "Mode 1" will be considered below as a representative case.

Fig. 5(a) shows the eigenfrequency of "Mode 1" and the temperature measured by thermal sensor I of Fig. 1 over a 24 h period centered at 143 h, after corrupting both traces with white Gaussian noise at standard deviations set to 4% of their respective maximum excursions in the "dynamic" thermal equilibrium phase. Note that for actual measurement systems the signal to noise ratios can vary widely and depend on a number of factors, most of which being related to intrinsic characteristics of the sensing equipment and the data acquisition instrumentation, hence the noise levels adopted for the numerical data considered in this article are simply set with the intention to hinder the detection of damage. Indeed, the shift in frequency occurring at 143 h and caused by the introduction of damage is now well-hidden within the added noise. The plot shows that there exists an inverse relation between eigenfrequency and temperature, and this is expected since (1) the material properties of Table 1 soften as temperature increases and (2) a temperature increase generates compressive stresses within the axially restrained beam that further soften the structural stiffness [31]. Fig. 5(c) displays the same data of Fig. 5(a) in the form of a "temperature vs frequency" scatter plot, while Fig. 5(b) shows the analogous plot obtained when using the noiseless data. Due to the differences in shape and phase between the measured time-series of temperature and frequency, each scatter plot draws an hysteresis-like loop, hence poor linear correlation between simultaneous measurements of temperature and frequency is expected. Note that in the noiseless scenario of Fig. 5(b) the sustained downward frequency shift is visually evident, while in the noise-added case of Fig. 5(c) it is much less obvious.

4.2.1. Case study C1: temperature compensation

The algorithm described in Section 2 was applied to both noiseless and noise-added temperature and modal data that are partially plotted in Fig. 5. As indicated in Fig. 3(a), the first 25 h of data were discarded to make sure that the initial "transient" stage was fully resolved and not included in the baseline period. The data acquired between 25 and 90 h of simulation were used as baseline to train the regression models, while that in the ranges 90–143 and 143–192 h formed undamaged and damaged monitoring datasets, respectively.

Fig. 6 compares the performance offered by LR and MLR trained with different lengths of temperature sequences. The performance is evaluated in terms of coefficient of determination R^2 (Eq. (2)) between measured and predicted values of frequency over baseline, undamaged and damaged monitoring datasets. Note that the horizontal axes of the plots indicate the "time lag" spanned by the temperature sequences input to the multiple regression. Since such time lag is expressed in minutes, and since the synthetic measurements are sampled every minute, the reported values directly correspond to the number of "past" temperature readings n used in Eq. (1) in addition to the temperature

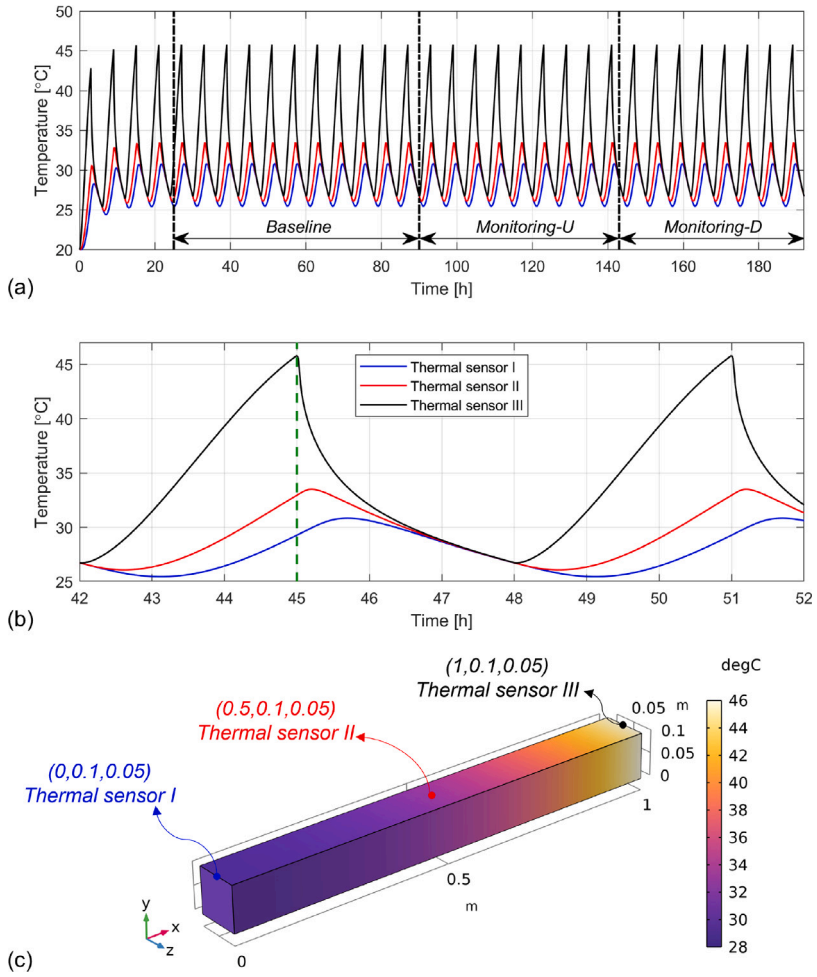

Fig. 3. (a) Temperature measured by thermal sensors I to III; the plot also shows the time-frames used to split the data into baseline and monitoring periods, where "Monitoring-U" and "Monitoring-D" stand for undamaged and damaged monitoring phases, respectively. (b) Zoomed view over a 10 h-period of plot (a), also showing with a green dashed vertical line the time instant at which the temperature field is plotted in (c). The locations of thermal sensors I to III, also shown in Fig. 1, are displayed in (c).

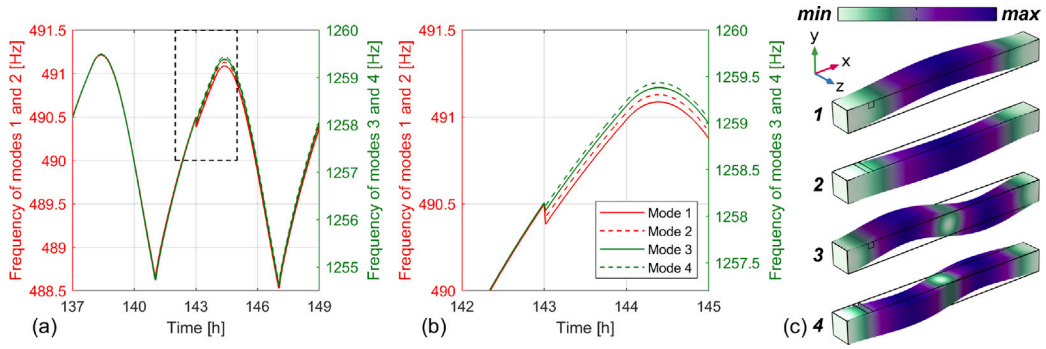

Fig. 4. Case study C1. (a, b) Lowest four eigenfrequencies; plot (b) zooms in the black rectangle of (a); left and right y-axes in each plot apply to modes 1–2 and 3–4, respectively. (c) Their associated mode shapes (the color scale represents the displacement magnitude).

measured simultaneously with the frequency. Therefore, the case of simple LR between temperature and frequency lies on the y-axis.

Fig. 6(a, b) pertain to the noiseless scenario, while Fig. 6(c, d) consider the traces corrupted with noise as described in the previous section. The right plots zoom in different areas of the corresponding left plots. As already suggested by the scatter plots seen in Fig. 5(b, c), Fig. 6(a, c) confirm that LR does not offer a satisfactory regression performance as it only yields R^2 values of roughly 45% for all three datasets and for both noiseless and noise-added scenarios.

Fig. 6(a, b) shows that when noiseless temperature and frequency data are considered, R^2 rapidly increases for all datasets as more past temperature data is used for the multiple regression operation, with the curves corresponding to baseline and undamaged monitoring datasets already reaching a value of 99.75% at $n = 10$. Past that value there are further marginal improvements, until an R^2 of exactly 100% is obtained for $n = 360$, i.e., when 6 h-long sequences of temperature history are given as input to MLR. This is consistent with the duration of the perfectly repeating heating periods used in the FE model, which translates to the fact that the regressor has nothing left to "learn" past

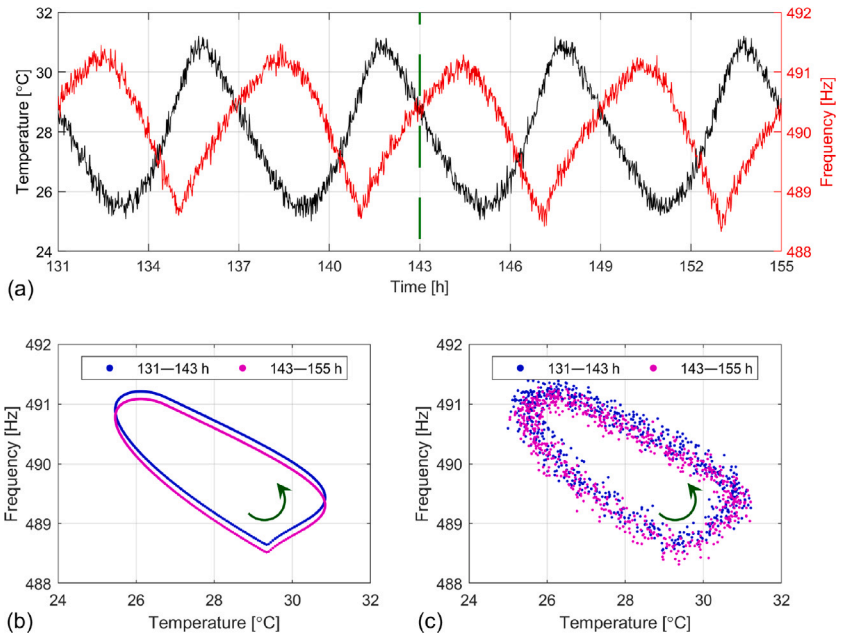

Fig. 5. Case study C1. (a) Noise-added eigenfrequency of "Mode 1" and temperature measured by thermal sensor I of Fig. 1; the green dashed line indicates the time of occurrence of damage. (b, c) "Temperature vs frequency" scatter plots produced using (b) noiseless and (c) noise-added data (note: the data used to produce (c) is the same data plotted in (a)); the green arrows indicate the direction of time.

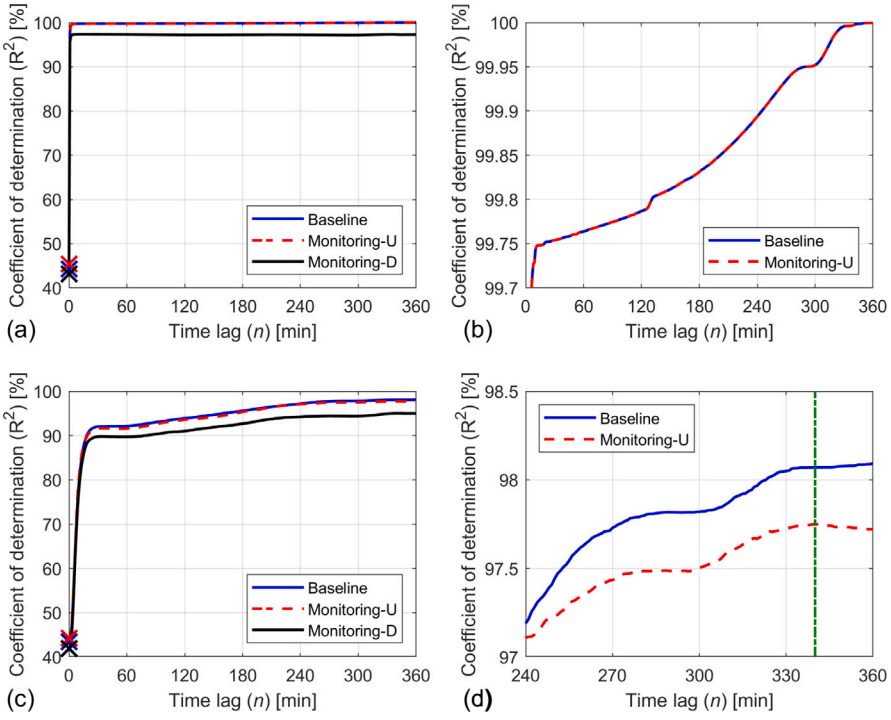

Fig. 6. Case study C1. R^2 as a function of past temperature values n used for multiple regression. Plots (a, b) and (c, d) refer to noiseless and noise-added scenarios, respectively. Plots (b) and (d) zoom in different areas of (a) and (c), respectively (the "Monitoring-D" curve does not appear at the zoom levels of (b, d)). LR corresponds to $n = 0$, and its R^2 values are marked with crosses. The green dash-dotted vertical line in (d) is at $n = 340$, the value used to produce the results in Fig. 7(b).

the 6 h mark. Fig. 7(a) superposes the actual eigenfrequency trace to that predicted by MLR with $n = 360$ in the noiseless scenario and over the same 24 h-period considered in Fig. 5. As indicated by the 100% R^2 value obtained in the undamaged monitoring dataset, the trained MLR can perfectly predict the modal frequency up to the occurrence of damage at 143 h. Once the structural conditions change, predicted and measured frequencies become offset, as expected (in fact, in Fig. 6(a, b) the curve corresponding to the damaged dataset is lower than the other two), and this can be exploited for damage detection. For comparison, Fig. 7(a) also plots the predictions from LR. As expected, they differ significantly from the measured data both before and after the introduction of damage, and do not exhibit any appreciable sensitivity to the changed structural conditions.

In the more realistic scenario of temperature and frequency data being corrupted with noise, which is investigated in Fig. 6(c, d), getting to an R^2 value of 100% is no longer possible. Nevertheless, the

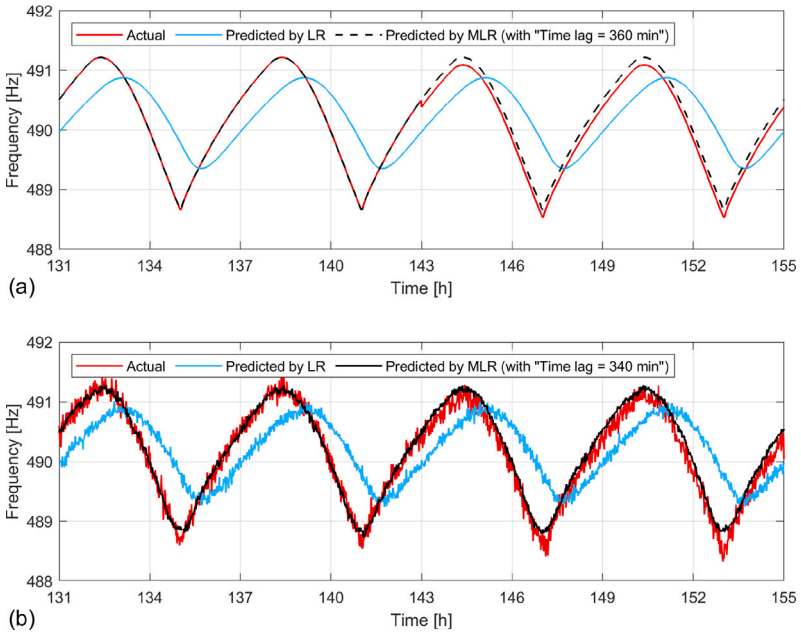

Fig. 7. Case study C1. Actual eigenfrequencies vs those predicted by LR and MLR in (a) noiseless and (b) noise-added scenarios over the same period considered in Fig. 5.

inclusion of past temperature data still proves highly beneficial, with R^2 growing steeply to about 90% at $\sim n = 20$ before embarking in a slower ascending path. The zoomed view given in Fig. 6(d) reveals that while the baseline trace keeps growing till the right end of the plot, the trace corresponding to undamaged monitoring starts a slowly descending path after $\sim n = 340$. This indicates that past that point there starts to be a negative balance between the very marginal additional information brought in by the increasingly longer temperature sequences and the noise affecting the baseline dataset to which MLR starts to overfit. It is then advantageous to choose an "optimal" n value for MLR roughly corresponding to the peak reached by the undamaged monitoring trace, e.g., $n = 340$ (which is indicated with a green dash-dotted vertical line in Fig. 6(d)). Note that in practical SHM applications this type of operation for the choice of an "optimal" n can be performed by splitting the baseline data in separate "training" and "validation" datasets, with the latter not actively taking part in the training procedure but only being used to provide an unbiased evaluation of the regression performance, in analogy to what is commonly done in the machine learning field (see e.g., [32]). Fig. 7(b) compares the actually measured eigenfrequencies to those predicted either by LR or by MLR with $n = 340$ in the noise-added scenario. Similarly as for the noiseless case of Fig. 7(a), the predictions of LR differ significantly from the measured values, while those of MLR are still very accurate, although the presence of noise makes it more challenging to detect the possible presence of small deviations between measured and MLR-predicted traces, such as those existing after 143 h.

In practical monitoring scenarios, a routine must be devised to perform an automated and continuous inspection of the incoming data and to flag cases in which predicted and measured values start to be dissimilar in a sustained manner, an occurrence that can be linked to the insurgence or growth of damage, as in the case of Fig. 7(b) past the 143 h mark. This can be accomplished by computing the squared difference (SD) between incoming pairs of predicted and actual eigenfrequencies and by then running a moving average on the SD trace in order to reduce the variability due to noise. When this procedure is employed on the data of Fig. 7(b) using a sliding window of 780 datapoints (corresponding to 13 h of monitoring data at the employed 60 s-sampling interval) to perform a trailing moving average operation, the blue curve shown in Fig. 8(b) is obtained. The trace remains essentially flat over both baseline and undamaged monitoring periods, before growing significantly after the introduction of damage at 143 h. In order to fully automatize the monitoring procedure, a threshold must be set, such that any crossing above it would raise an alarm. Care must be taken when deciding on an appropriate threshold value, which should be high enough to minimize the number of false calls, but not too high as to miss the signatures of actual damage. As a matter of example the threshold in Fig. 8(b) was set as twice the largest value returned by the moving average operator within the baseline set. By using such threshold this damage would have been automatically detected at ~152 h, i.e., roughly 9 h after its first appearance. For comparison, Fig. 8(a) considers the case in which LR is used to predict eigenfrequency data. As seen in Fig. 7(a), the predictions from LR are poor estimates of the actual values, hence the moving averages of the squared differences are significantly higher than those seen in Fig. 8(b). Such values remain almost unchanged after damage has occurred, hence such damage would remain undetected.

4.3. Case study C2: strain data

Fig. 9(a) shows temperature and strain measured by thermal sensor III and strain gauge I of Fig. 1, respectively, over a 24 h period centered at the time of introduction of the differential settlement in case study C2. Note that strains are considered positive when they are tensile, are given in parts per million (i.e., in microstrains ($\mu\varepsilon$)), and are referenced to the initial undeformed structural configuration. The overall upward shift of the measured values towards the ~125–250 microstrain variation seen in Fig. 9(a) occurs over the first ~18 h of simulation time, i.e., the time required to reach the "dynamic" thermal equilibrium as discussed in Section 4.1. The figure shows that there exists a significant time lag between temperature and strain data, since they are measured at two locations being almost one meter apart, and the shapes of the two traces are also different. The effects of the differential settlement at 143 h are immediately registered as a small upward shift in the strain history, which is then carried forward for the remainder of the simulation.

Detecting the change induced by the simulated differential settlement is significantly more challenging when the traces are affected by measurement noise. In particular, Fig. 9(b) plots the same 24 h period of temperature and strain histories as in Fig. 9(a) after corrupting them with white Gaussian noise at standard deviations set to 4% of

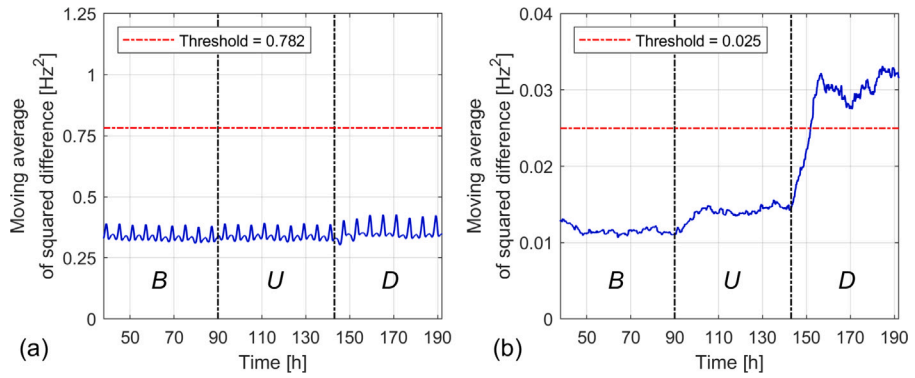

Fig. 8. Case study C1. Moving averages of the SDs between actual eigenfrequencies and those predicted by (a) LR and (b) MLR with $n = 340$ in the noise-added scenario. The x-axes start at 38 h, i.e., after the moving average is fully initialized. The black vertical lines indicate the times of transition between baseline (B), undamaged (U) and damaged (D) monitoring sets. Note that the zoom-level in the y-axis of (a) is different than that of (b).

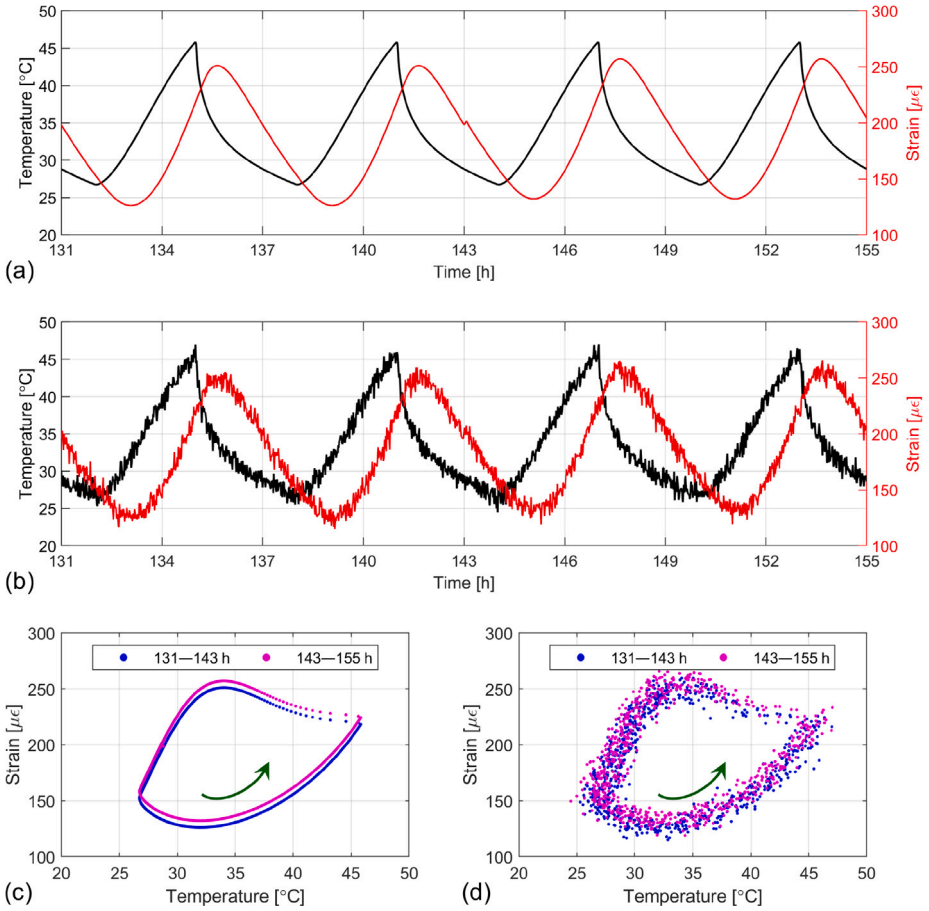

Fig. 9. Case study C2. (a) Noiseless and (b) noise-added temperature and strain traces measured by thermal sensor III and strain gauge I of Fig. 1. (c, d) "Temperature vs strain" scatter plots using the same data shown in (a, b), respectively; the green arrows indicate the direction of time.

the temperature and strain maximum excursions, respectively, in the "dynamic" thermal equilibrium phase. This procedure is analogous to that operated on the signals of case study C1 and discussed in Section 4.2.

The same data of Fig. 9(a, b) is shown in Fig. 9(c, d), respectively, in the form of "temperature vs strain" scatter plots. Due to the discussed differences in shape and phase between the two traces, a rather wide hysteresis-like loop appears, hence poor linear correlation is expected. Again, in the noiseless scenario of Fig. 9(c) the sustained upward strain shift is visually evident, while in the noise-added case of Fig. 9(d) it is much less obvious.

4.3.1. Case study C2: temperature compensation

The algorithm of Section 2 was tested on both noiseless and noise-added temperature and strain data that are partially plotted in Fig. 9. Each of the two datasets was split in baseline, undamaged and damaged monitoring sets using the same rules adopted in Section 4.2.1, i.e., the three periods are 25–90, 90–143 and 143–192 h, respectively.

Fig. 10 is analogous to Fig. 6. In particular, Fig. 10(a, b) pertain to the noiseless scenario, while Fig. 10(c, d) consider the traces corrupted with noise, with the right plots zooming in different areas of the corresponding left plots. In this case study, LR provides even lower R^2 values than those seen in case study C1 (i.e., R^2 =~2% for all three

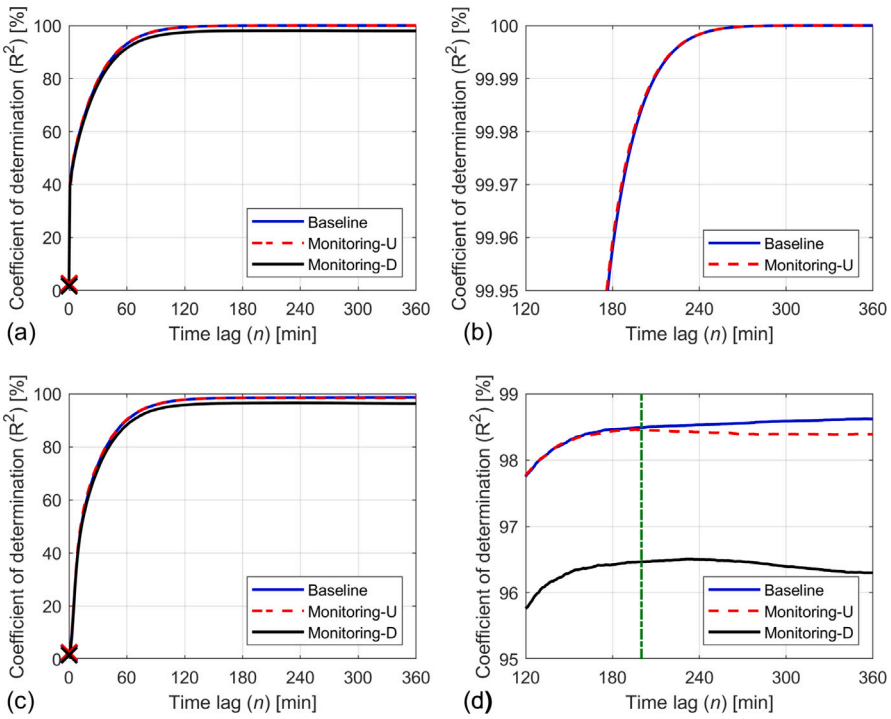

Fig. 10. Case study C2. R^2 as a function of past temperature values n used for multiple regression. Plots (a, b) and (c, d) refer to noiseless and noise-added scenarios, respectively. Plots (b) and (d) zoom in different areas of (a) and (c), respectively (the "Monitoring-D" curve does not appear at the zoom level of (b)). R^2 values of LR are marked with crosses. The green dash-dotted vertical line in (d) is at $n = 200$, the value used to produce the results in Fig. 11(b).

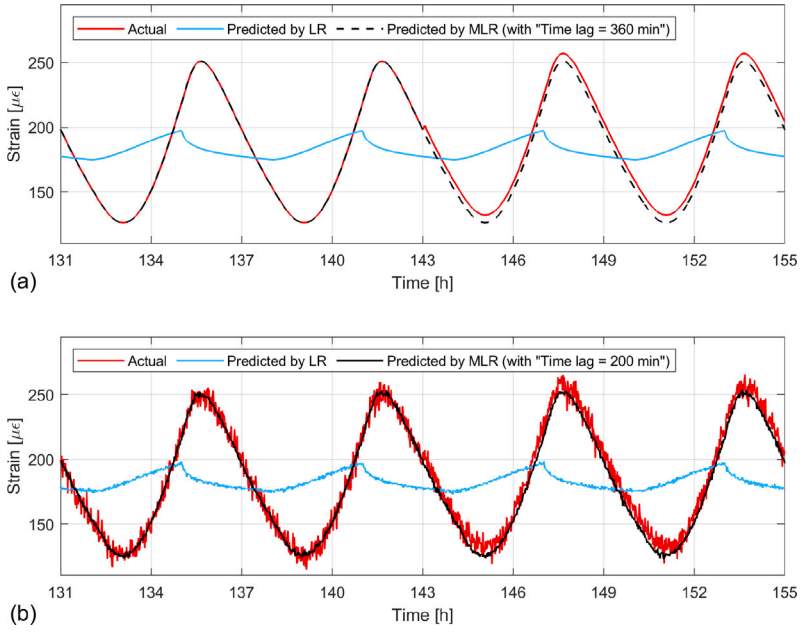

Fig. 11. Case study C2. Actual strains vs those predicted by LR and MLR in (a) noiseless and (b) noise-added scenarios over the same period considered in Fig. 9.

datasets and for both noiseless and noise-added scenarios), and this was already suggested by the hysteresis loops of Fig. 9(c, d) being wider than those of Fig. 5(b, c). Indeed, the strains predicted by LR shown in Fig. 11 are very far off from the actually measured values.

For the noiseless temperature and strain data (Fig. 10(a, b)), R^2 monotonically increases for all datasets as more past temperature data is used for the multiple regression operation. Both traces corresponding to baseline and undamaged monitoring datasets reach a value of 99.96% roughly at $n = 180$. Past that value there are further marginal improvements, which becomes not visible at the zoom level of Fig. 10(b) for n higher than ~270, until an R^2 of exactly 100% is obtained for $n = 360$, i.e., when 6 h-long sequences of temperature history are given as input to MLR. Indeed, Fig. 11(a) confirms that by training MLR with $n = 360$ over the baseline data, strain can be perfectly predicted until the differential settlement occurs at 143 h, at which point predicted and measured strains become offset.

When noise is added to temperature and strain data (Fig. 10(c, d)), Fig. 10(d) shows that in this case the curve pertaining to the undamaged monitoring dataset already starts to descend at $\sim n = 200$, a point that is indicated by the green dash-dotted vertical line. Therefore,

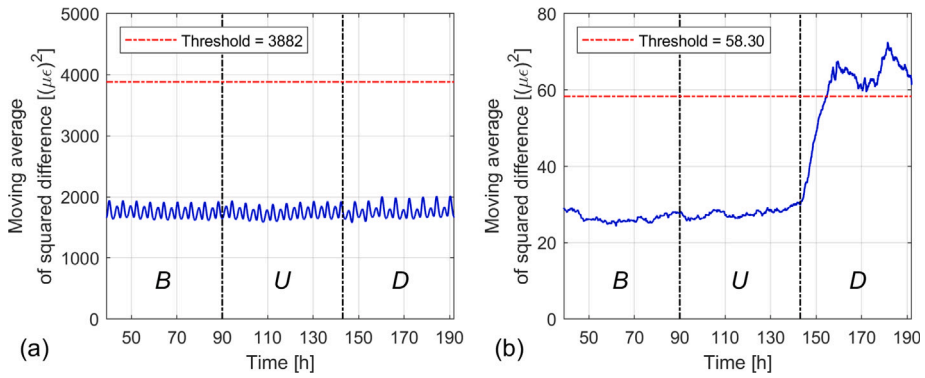

Fig. 12. Case study C2. Moving averages of the SDs between measured strains and those predicted by (a) LR and (b) MLR with $n = 200$ in the noise-added scenario. The x-axes start at 38 h, i.e., after the moving average is fully initialized. The black vertical lines are as in Fig. 8. Note that the zoom-level in the y-axis of (a) is different than that of (b).

$n = 200$ is selected as the "optimal" value for MLR training in this scenario, and Fig. 11(b) compares actual strains to those predicted by MLR with this n choice. Again, the predictions during the undamaged monitoring period are a close match to the measured values. The presence of noise hinders the detection of the small sustained change occurring after 143 h, and the use of an averaging operator is expected to help. Indeed, the trailing moving average computed on the SDs between predicted and actual strains using a sliding window of 780 datapoints, which is plotted in Fig. 12(b), registers a rapid growth after the introduction of damage at 143 h and crosses the threshold (which was set according to the rule proposed in Section 4.2.1) roughly 11 h after damage occurred. For comparison, Fig. 12(a) plots the moving average run on the SDs obtained when using LR to predict strain data. Analogously to what already seen in case study C1 (Fig. 8), the values in the baseline and undamaged monitoring periods of Fig. 12(a) are significantly higher than those of Fig. 12(b), and the trace does not increase in any significant manner after damage occurs at 143 h, hence the considered differential settlement would remain undetected.

5. Experimental case study: KW51 bridge

Finally, the temperature compensation method of Section 2 is tested over some open-access experimental data acquired from the KW51 bridge in Leuven, Belgium [22]. This is a 115 m-long steel bowstring railway bridge instrumented with various sensors including a thermocouple and a set of accelerometers (please refer to [33] for a detailed description of the bridge and the monitoring system, including the exact locations of the sensors). Fourteen modal frequencies were estimated at hourly interval from the recorded ambient vibration data using the reference-based covariance-driven stochastic subspace identification (SSI-cov/ref) algorithm [33,34]. The thermocouple was set to record temperature at the same hourly rate. Note that the material properties of steel, from which the KW51 bridge is constructed, exhibit a different temperature dependence than those of the aluminum considered for the numerical case studies, which are reported in Table 1. An example of the expected variation in the Young's modulus of steel over a ~60 °C temperature range can be found in Fig. 1(b) of [35].

As a representative example, the analysis discussed in this section considers the first mode, which involves the lateral motion of the arches [33], and a period of data acquisition of almost 3 months. Such period starts on 30 September 2019, i.e., after the bridge was retrofitted to resolve a construction error, and ends on 19 December 2019, i.e., just before a ~3 day-gap in the data collection that occurred, presumably for a malfunctioning of the monitoring system, a few days before the end of the available open-access dataset. The modal data also contained some shorter gaps scattered within the considered period, and these missing entries were filled using the nearest non-missing values. While this is a standard, basic method to handle missing data, more advanced techniques have recently been proposed for data imputation in SHM, such as that reported in [36]. Finally, note that no damage was artificially added to the bridge nor was reported to occur "naturally".

Fig. 13(a) plots the first eigenfrequency and the temperature measured by the thermocouple over the considered ~3 month-period. The thermal data shows a ~22 °C excursion with minimum readings just above 0 °C. The modal data is affected by rather high levels of noise, whose amplitude vary significantly over time, and this was mainly attributed to electromagnetic interferences with the high-voltage railway electrification [33]. An in-depth analysis of such data reveals that the true underlying modal variation ranges between ~0.508 and ~0.512 Hz across this temperature range. Note that such low signal-to-noise ratio limits the maximum value of R^2 that can possibly be achieved on this dataset, since the variability of the measured data solely due to random noise will necessarily remain unaccounted for [25].

The data acquired before 26 October 2019 were used as baseline to train the regression models, and Fig. 13(b) plots the R^2 values between measured and predicted eigenfrequencies over baseline and monitoring datasets. Similarly as in Figs. 6 and 10, the horizontal axis indicates the time lag, here expressed in hours, spanned by the temperature sequences input to the multiple regression. Since measurements are sampled every hour, the reported values again directly correspond to the number of "past" temperature readings n used in Eq. (1). LR yields an R^2 value of about 13% on the baseline data used for its training, and its ability to predict the expected eigenfrequencies based on temperature measurements is extremely poor, as indicated by an R^2 of ~1.5% obtained over the monitoring period. As longer temperature sequences are used for multiple regression operations, R^2 increases for both datasets until peaking at values close to 22% roughly at $n = 5$, corresponding to 5 h of temperature history. Then, for higher n values the trace pertaining to the monitoring dataset slowly starts to descend, while the baseline's curve keeps ascending, indicating the start of overfitting to noise, as explained in the previous sections. Therefore, $n = 5$ is selected as the "optimal" value for MLR training in this scenario.

Fig. 13(c, d) zoom on two ~5 day-periods over which the noise levels remained a little lower than elsewhere, thus enabling to better appreciate how close (or far off) the eigenfrequencies predicted by either LR or MLR are to the actually measured values. Notably, despite the training over the very noisy baseline data, the predictions of MLR fed with 5 h-long sequences of temperature are very well adherent to the measured eigenfrequencies, while the LR-predicted trace offers a much poorer performance by remaining largely offset from the latter.

As explained in Section 4.2.1, from a practical perspective, the eigenfrequencies predicted by MLR as new measurements are acquired can serve as input for an automated damage detection algorithm. This can be achieved, for instance, using the routine described in Sections 4.2.1 and 4.3.1, which involves setting a threshold on the moving average of the squared differences between predicted and measured eigenfrequencies.

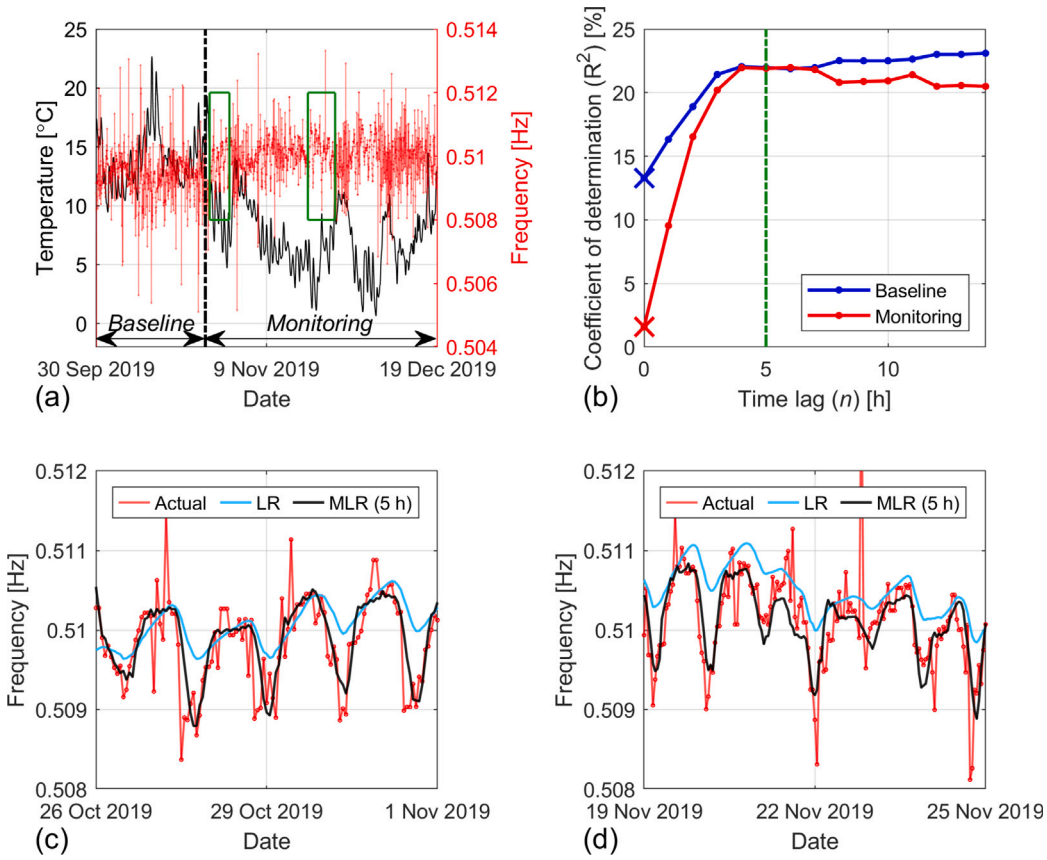

Fig. 13. Experimental case study. (a) First eigenfrequency and temperature measured over the considered ~3 month-period. (b) R^2 as a function of past temperature values n used for multiple regression; LR corresponds to n = 0, and its R^2 values are marked with crosses. (c, d) Actual eigenfrequencies vs those predicted by LR and MLR over the two periods indicated by the green rectangles in (a).

6. Conclusions

A novel temperature compensation method has been discussed and evaluated over two numerical and an experimental monitoring case studies. The method is based on the observation that a regression model between instantaneous measurements of temperature and structural response cannot accurately capture their interrelation, since the materials' thermal inertia essentially act as a filter between the two. Therefore, the proposed method uses long sequences of temperature measurements as independent variables for multiple linear regression (MLR), effectively giving MLR sufficient information to model the heat transfer phenomena occurring within the structure and, hence, to predict the structural response. In all considered case studies temperature measurements were acquired at a single structural location, and were paired with either a "global" structural parameter (i.e., a natural frequency of vibration) or a "local" one (i.e., strain). The results obtained on all datasets, and, for the numerical case studies, on both a noiseless and a noise-added scenario, showed an excellent performance when MLR was fed with sufficiently long temperature sequences, strongly outperforming the standard use of instantaneous temperature measurements. This confirms that the proposed method can be successfully applied to predict both global and local structural responses.

Furthermore, the comparison of the results obtained on the numerical datasets for noiseless and noise-added scenarios shed some lights on the "optimal" length of sequential temperature data to be used as input for MLR. First, the results on the noiseless datasets showed that there cannot be any added benefit in increasing the input sequential temperature length once that is long enough to capture all heat transfer phenomena occurring within the structure. However, the analyses on the noise-added scenarios also showed that there exists a trade-off between the additional information that can be learned by the regressor by increasing the length of the input temperature sequences and the detrimental effect of measurement noise to which MLR would increasingly tend to overfit. Therefore, a case-specific and data-driven procedure for the estimation of an "optimal" input temperature length was suggested, and this requires splitting the baseline data used to train the regressor into a proper training and a validation dataset, where the latter can be used to unbiasedly test the regressor performance.

Finally, it is important to emphasize that since the method is purely data-driven, it can be readily applied to any real-world monitoring system where at least one thermocouple is installed on the monitored structure. When multiple thermocouples are available, various options exist for utilizing the additional information. For example, one approach would be to run multiple instances of the algorithm independently on the sequences acquired by each thermocouple, thereby providing redundancy in the predicted structural responses, which can then be compared to the actual measurements.

CRediT authorship contribution statement

S. Mariani: Writing – review & editing, Writing – original draft, Visualization, Supervision, Software, Project administration, Methodology, Investigation, Formal analysis, Data curation, Conceptualization. **F. Zeighami:** Writing – review & editing, Validation, Formal analysis. **A. Kalantari:** Formal analysis. **S. Kamali:** Writing – review & editing, Formal analysis. **S. de Miranda:** Writing – review & editing, Resources. **A. Marzani:** Writing – review & editing, Resources.

Declaration of competing interest

The authors declare that they have no known competing financial interests or personal relationships that could have appeared to influence the work reported in this paper.

Acknowledgments

The first author is grateful to the "Programma per Giovani Ricercatori Rita Levi Montalcini year 2020" (grant PGR20WNZMY) of the Italian Ministry of University and Research (MUR) for the financial support. The first author is also grateful to Prof. Antonio Palermo for the helpful discussion on modeling of damage.

Appendix. Transient linear thermoelastic problem

The transient linear thermoelastic problem is here recalled. Consider an elastic isotropic body occupying a closed and bounded region whose boundary and open set are denoted $\partial\Omega$ and Ω, respectively. The position vector $\mathbf{x}$ indicates a point of the domain in a given Cartesian coordinate system, while t is time. The heat transfer problem is described by the temperature T and by the heat flux vector $\mathbf{q}$. Temperature and heat flux are prescribed on the parts $\partial\Omega_T$ and $\partial\Omega_q$ of the body's boundary ($\partial\Omega_T \cap \partial\Omega_q = 0$, $\partial\Omega_T \cup \partial\Omega_q = \partial\Omega$), respectively. In the absence of internal heat generation, the problem is ruled by the following equations in Ω:

$$k\nabla^2 T = \rho c \dot{T} \tag{A.1}$$

$$\mathbf{q} = -k\nabla T \tag{A.2}$$

which express the heat diffusion equation and the constitutive law (i.e., Fourier's law [8]), respectively. In Eqs. (A.1)–(A.2) k, ρ and c are the material's thermal conductivity, density and specific heat, respectively.

The heat flux on $\partial\Omega_q$ can be either directly specified or set as resulting from convective and/or radiative phenomena. Convection combines the effects of conduction between the boundaries of the body and the adjacent fluid to that of fluid motion. This phenomenon is described by Newton's law of cooling as:

$$\mathbf{q}^c = h^c \left(T - T^F\right) \hat{\mathbf{n}} \tag{A.3}$$

where $\mathbf{q}^c$ is the heat flux vector due to convection, h^c is the convective heat transfer coefficient, T is the body's temperature at the boundary, T^F is the temperature of the fluid sufficiently far from the body's boundary and $\hat{\mathbf{n}}$ is the unit normal vector pointing into the fluid. Radiative boundary conditions are not used in the model described in this work.

The thermoelastic configuration of the body at a given time instant t is described by the displacement vector $\mathbf{u}$, and by the strain and stress tensors $\boldsymbol{\varepsilon}$ and $\boldsymbol{\sigma}$, respectively. The displacements and the surface tractions are prescribed on the parts $\partial\Omega_u$ and $\partial\Omega_p$ of the body's boundary ($\partial\Omega_u \cap \partial\Omega_p = 0$, $\partial\Omega_u \cup \partial\Omega_p = \partial\Omega$), respectively. Let $T_I = T_I(\mathbf{x}, t_I)$ and $T_0 = T_0(\mathbf{x}, t_0)$ indicate the temperature fields within the body at time instants t_I and t_0, with $t_I > t_0$. The thermal strain $\boldsymbol{\varepsilon}^T(\mathbf{x})$ due to the field of temperature change $\Delta T(\mathbf{x}) = T_I - T_0$ is given by:

$$\boldsymbol{\varepsilon}^T(\mathbf{x}) = \alpha \Delta T(\mathbf{x}) \mathbf{I} \tag{A.4}$$

where α is the material's linear thermal expansion coefficient and $\mathbf{I}$ is the identity matrix. In the absence of body forces, the quasi-static thermoelastic problem is governed by the following equations:

$$\boldsymbol{\varepsilon} = \frac{1}{2}\left(\nabla\mathbf{u} + (\nabla\mathbf{u})^T\right) \tag{A.5}$$

$$\nabla \cdot \boldsymbol{\sigma} = 0 \tag{A.6}$$

$$\boldsymbol{\sigma} = \mathbb{C}\left(\boldsymbol{\varepsilon} - \alpha \Delta T \mathbf{I}\right) \tag{A.7}$$

which express the strain–displacement relationship, the equilibrium equations and the constitutive law, respectively. In Eq. (A.7) $\mathbb{C}$ is the elastic moduli tensor.

In this work $\mathbb{C} = \mathbb{C}(T)$ and $\alpha = \alpha(T)$, i.e., the temperature field existing within the body at any given time instant also influences the structural response by varying the material properties. Furthermore, thermally-induced strains and stresses influence the structural modal parameters [31,37].

Data availability

Data will be made available on request.

References

[1] Lynch JP, Loh KJ. A summary review of wireless sensors and sensor networks for structural health monitoring. Shock Vib Dig 2006;38(2):91–130.
[2] Sohn H, Farrar CR, Hemez FM, Shunk DD, Stinemates DW, Nadler BR, et al. A review of structural health monitoring literature: 1996–2001. Los Alamos Natl Lab USA 2003;1:16.
[3] Farrar CR, Worden K. Structural health monitoring: A machine learning perspective. John Wiley & Sons; 2012.
[4] Sohn H. Effects of environmental and operational variability on structural health monitoring. Philos Trans R Soc A: Math Phys Eng Sci 2007;365(1851):539–60.
[5] Catbas FN, Susoy M, Frangopol DM. Structural health monitoring and reliability estimation: Long span truss bridge application with environmental monitoring data. Eng Struct 2008;30(9):2347–59.
[6] Xia Y, Chen B, Weng S, Ni Y-Q, Xu Y-L. Temperature effect on vibration properties of civil structures: a literature review and case studies. J Civ Struct Heal Monit 2012;2:29–46.
[7] Koo K-Y, Brownjohn J, List D, Cole R. Structural health monitoring of the tamar suspension bridge. Struct Control Heal Monit 2013;20(4):609–25.
[8] Cengel RA. Introduction to thermodynamics and heat transfer. McGraw-Hill; 2008.
[9] Boley BA, Weiner JH. Theory of thermal stresses. Courier Corporation; 2012.
[10] Guo T, Liu J, Zhang Y, Pan S. Displacement monitoring and analysis of expansion joints of long-span steel bridges with viscous dampers. J Bridg Eng 2015;20(9):04014099.
[11] Gong X, Song X, Cai C, Li G, Xiong W. A temperature-driven approach for quantitative assessment of strengthening effect of continuous bridges using structural health monitoring data. Struct Heal Monit 2023;14759217231181882.
[12] Chen C, Wang Z, Wang Y, Wang T, Luo Z, et al. Reliability assessment for PSC box-girder bridges based on SHM strain measurements. J Sensors 2017;2017.
[13] Yang K, Ding Y, Sun P, Zhao H, Geng F. Modeling of temperature time-lag effect for concrete box-girder bridges. Appl Sci 2019;9(16):3255.
[14] Sohn H, Dzwonczyk M, Straser EG, Kiremidjian AS, Law KH, Meng T. An experimental study of temperature effect on modal parameters of the alamosa canyon bridge. Earthq Eng Struct Dyn 1999;28(8):879–97.
[15] Marill KA. Advanced statistics: linear regression, part II: multiple linear regression. Acad Emerg Med 2004;11(1):94–102.
[16] Peeters B, De Roeck G. One-year monitoring of the Z24-Bridge: environmental effects versus damage events. Earthq Eng Struct Dyn 2001;30(2):149–71.
[17] Ljung L. System identification. In: Signal analysis and prediction. Springer; 1998, p. 163–73.
[18] Kromanis R, Kripakaran P. Data-driven approaches for measurement interpretation: analysing integrated thermal and vehicular response in bridge structural health monitoring. Adv Eng Informatics 2017;34:46–59.
[19] Wang C, Ansari F, Wu B, Li S, Morgese M, Zhou J. LSTM approach for condition assessment of suspension bridges based on time-series deflection and temperature data. Adv Struct Eng 2022;25(16):3450–63.
[20] Hochreiter S, Schmidhuber J. Long short-term memory. Neural Comput 1997;9(8):1735–80.
[21] Mariani S, Kalantari A, Kromanis R, Marzani A. Data-driven modeling of long temperature time-series to capture the thermal behavior of bridges for SHM purposes. Mech Syst Signal Process 2024;206:110934.
[22] Maes K, Lombaert G. Monitoring data for railway bridge KW51 in Leuven, Belgium, before, during, and after retrofitting. Zenodo; 2020, http://dx.doi.org/10.5281/zenodo.3745914.
[23] Comanducci G, Magalhães F, Ubertini F, Cunha Á. On vibration-based damage detection by multivariate statistical techniques: Application to a long-span arch bridge. Struct Heal Monit 2016;15(5):505–24.
[24] Huang M, Zhang J, Hu J, Ye Z, Deng Z, Wan N. Nonlinear modeling of temperature-induced bearing displacement of long-span single-pier rigid frame bridge based on DCNN-LSTM. Case Stud Therm Eng 2024;53:103897.

[25] Casella G, Berger RL. Statistical inference. Cengage Learning; 2021.
[26] of Defense USD. Military handbook: metallic materials and elements for aerospace vehicle structures, v. 1, U.S. Department of Defense; 1990.
[27] Li L, Chen B, Zhou L, Xia Q, Zhou Y, Zhou X, et al. Thermal behaviors of bridges—A literature review. Adv Struct Eng 2023;26(6):985–1010.
[28] Brincker R, Ventura C. Introduction to operational modal analysis. John Wiley & Sons; 2015.
[29] COMSOL, Inc. COMSOL multiphysics reference manual, version 5.6. 2020, www.comsol.com.
[30] Garvin JW. A student's guide to the Navier-Stokes equations. Cambridge University Press; 2023.
[31] Lieven NA, Greening P. Effect of experimental pre–stress and residual stress on modal behaviour. Philos Trans R Soc Lond Ser A Math Phys Eng Sci 2001;359(1778):97–111.
[32] Géron A. Hands-on machine learning with Scikit-Learn, Keras, and TensorFlow. "O'Reilly Media, Inc."; 2022.
[33] Maes K, Lombaert G. Monitoring railway bridge KW51 before, during, and after retrofitting. J Bridg Eng 2021;26(3):04721001.
[34] Peeters B, De Roeck G. Reference-based stochastic subspace identification for output-only modal analysis. Mech Syst Signal Process 1999;13(6):855–78.
[35] Huang M-S, Gül M, Zhu H-P. Vibration-based structural damage identification under varying temperature effects. J Aerosp Eng 2018;31(3):04018014.
[36] Huang M, Wan N, Zhu H. Reconstruction of structural acceleration response based on CNN-BiGRU with squeeze-and-excitation under environmental temperature effects. J Civ Struct Heal Monit 2024;1–19.
[37] Mottershead J, Mares C, Friswell M, James S. Selection and updating of parameters for an aluminium space-frame model. Mech Syst Signal Process 2000;14(6):923–44.